Available online at www.sciencedirect.com
ScienceDirect
Journal of Solid State Chemistry 180 (2007) 1306–1317
JOURNAL OF SOLID STATE CHEMISTRY
www.elsevier.com/locate/jssc

Lithium conductivity in an Li-bearing double-ring silicate mineral, sogdianite

S.-H. Park[a,*], M. Hoelzel[b,c], H. Boysen[a], E. Schmidbauer[d]

[a]Section Crystallography, Earth and Environmental Sciences, Ludwig-Maximilians-Universität München, Germany
[b]Material- and Earthsciences, Technische Universität Darmstadt, Germany
[c]Forschungsneutronenquelle Heinz Maier-Leibnitz (FRMII), Garching, Germany
[d]Section Geophysics, Earth and Environmental Sciences, Ludwig-Maximilians-Universität München, Germany

Received 16 November 2006; received in revised form 15 January 2007; accepted 4 February 2007
Available online 17 February 2007

Abstract

The crystal structure of an Li-bearing double-ring silicate mineral, sogdianite ($(Zr_{1.18}Fe^{3+}_{0.55}Ti_{0.24}Al_{0.03})(\Upsilon_{1.64},Na_{0.36})K_{0.85}[Li_3Si_{12}O_{30}]$, $P6/mcc$, $a \approx 10.06$ Å, $c \approx 14.30$ Å, $Z = 2$), was investigated by neutron powder diffraction from 300 up to 1273 K. Rietveld refinements of displacement parameters revealed high anisotropic Li motions perpendicular to the crystallographic c-axis, indicating an exchange process between tetrahedral $T2$ and octahedral A sites. AC impedance spectra of a sogdianite single crystal ($0.04 \times 0.09 \times 0.25\,cm^3$) show that the material is an ionic conductor with conductivity values of $\sigma = 4.1 \times 10^{-5}\,S\,cm^{-1}$ at 923 K and $1.2 \times 10^{-3}\,S\,cm^{-1}$ at 1219 K perpendicular to the c-axis, involving two relaxation processes with activation energies of 1.26(3) and 1.08(3) eV, respectively.

Keywords: Sogdianite; Lithium; Conductivity; Neutron diffraction; Rietveld refinement; AC impedance; Double-ring silicates; Milarite; Structure

1. Introduction

Sogdianite $(Zr,Ti,Fe^{3+},Al)_2(\Upsilon,Na)_2K_1[Li_3Si_{12}O_{30}]$ (Υ = vacancy) [1,2] and other Li-bearing double-ring silicates are of high interest as potential materials in which either lithium interstitials or vacancies can be created for fast Li-ionic conduction. These naturally occurring materials are derivatives of the milarite type of minerals showing hexagonal or pseudo-hexagonal symmetry with the general formula $^{[6]}A_2\ ^{[9]}B_2\ ^{[12]}C\ ^{[18]}D[^{[4]}T2_3\ ^{[4]}Si_{12}O_{30}]$ where A = Al, Fe^{3+}, Sn^{4+}, Mg, Zr, Fe^{2+}, Ca, Na, (Y, REE); B = Na, H_2O, Υ; C = K, Na, Υ; $D = \Upsilon$; $T1$ = Si, Al; $T2$ = Li, Be, B, Mg, Al, Si, Mn^{2+}, Zn [3]. Characteristically, this type of structure can adopt a wide variety of cations besides Si^{4+} in the framework. The latter prefer to occupy the $T1$ site making up regular double 6-membered rings (6MRs) of SiO_4 tetrahedra (so-called "ring tetrahedra") (Fig. 1a). These double 6MRs are connected via highly distorted $T2O_4$ tetrahedra (ring-linking tetrahedra) to build up the tetrahedral framework. The topology produces four different tube- or cage-like voids of 6-, 9-, 12, and 18-coordinated A, B, C, and D sites, respectively (Fig. 1b). In the resulting fairly open framework, the D site is usually empty, while the B and C sites are occupied by water molecules, alkali, and alkaline-earth cations. Compared to zeolites, however, milarite-type materials are not capable of ion exchange due to the narrow openings of the cages. The octahedral site A, besides $T2$, allows this topology to possess great chemical and geometrical flexibility, since diverse multivalent cations can build AO_6 octahedra. Each AO_6 octahedron is edge-sharing to three ring-linking $T2O_4$ tetrahedra and corner-sharing to six ring $T1O_4$ tetrahedra (Fig. 1a). As these connections are formed layer-like parallel to the (001) plane, the AO_6 octahedra support the tetrahedral framework predominantly perpendicular to the c-axis.

Li-bearing milarite-family members contain Li at $T2$ with various A cations, e.g., in sogdianite ($A = Zr$), sugilite ($A = Fe^{3+}$), brannockite ($A = Sn^{4+}$), and Berezanskite

*Corresponding author. Sektion Kristallographie, Geo- und Umweltwisseschaften der LMU, Theresienstr. 41, 80333 München, Germany. Fax: +49 89 289 14015.
E-mail address: sohyun.park@lmu.de (S.-H. Park).

0022-4596/$ - see front matter © 2007 Published by Elsevier Inc.
doi:10.1016/j.jssc.2007.02.001

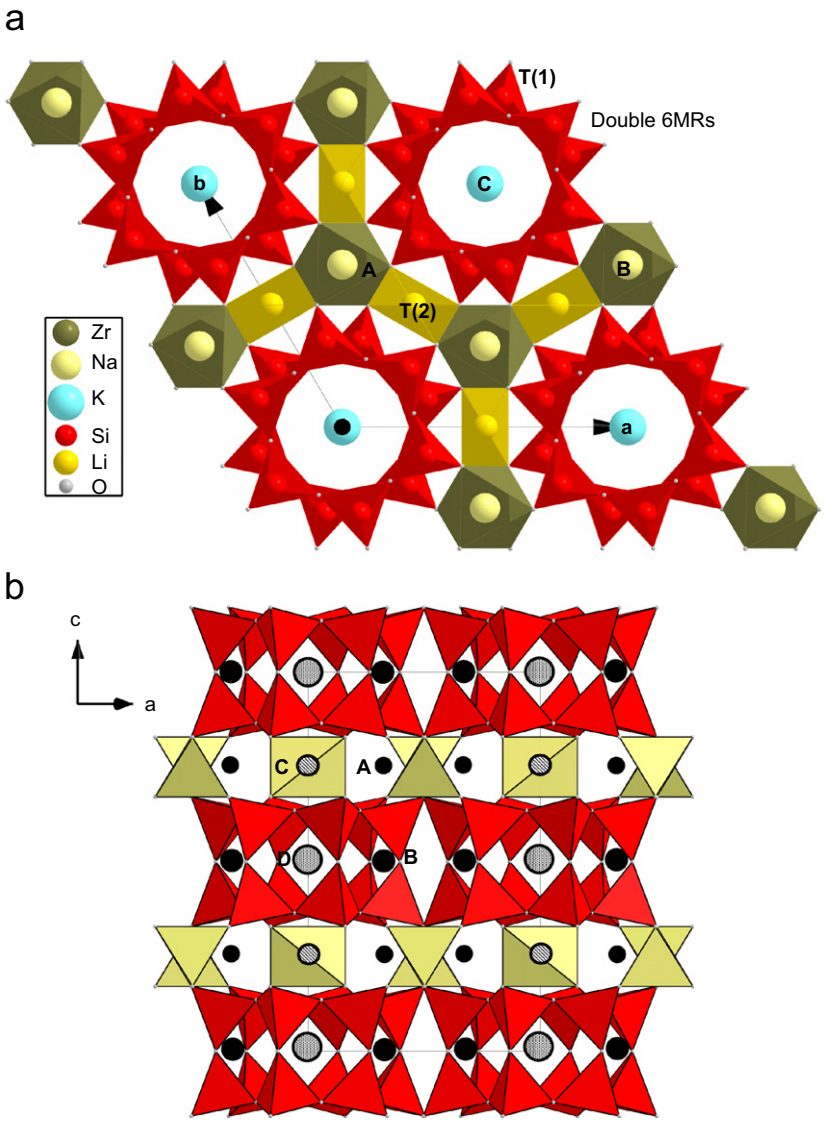

Fig. 1. (a) Projection of partial structure of sogdianite parallel to the *c*-axis, showing the connection of double 6MRs via $T2O_4$ tetrahedra. Each of these ring-linking $T2O_4$ tetrahedra is edge-sharing with two AO_6 octahedrons. Al, Ti^{4+}, Fe^{3+}, and Zr are statically disordered over those octahedral sites, while Na and K are located on more spacious *B* and *C* sites, respectively. *T*2 sites in sogdianite are exclusively occupied by Li. (b) Locations of various cage-like voids within the milarite-type topology in projection parallel to [010]. The [18]-coordinated *D* site is located at the center of each double 6MRs. The [12]-coordinated *C* site is found at the center of large $[Si_{12}O_{30}]$ cage formed by connection of double 6MRs over ring-linking tetrahedra parallel to the *c*-axis. Between such $[Si_{12}O_{30}]$ cages, lining up parallel to the *a*-axis, there is the octahedral site *A*. The [6 + 3]-coordinated *B* site resides directly below the *A* site in the [001] direction.

($A = Ti^{4+}$). As reported so far [1–6], in these Li-bearing double-ring silicates vacancies are rarely present at the *T*2 and *A* sites. In this case, any Li conduction, if present, would proceed at high temperatures by one-to-one site-exchanging processes such as $Li \leftrightarrow A \leftrightarrow Li$ via an interstitialcy mechanism. Three points are important to this view: the edge-sharing connection of AO_6 to $T2O_4$, provides short hopping distances (<3 Å); the interatomic bond lengths within the AO_6 octahedra ($d(A\text{–}O) = 1.97\text{–}2.1$ Å) are similar to those in the $T2O_4$ tetrahedra (d(Li–O) = 1.95~1.97 Å [1–6]); Li and those *A* cations can adopt both 4- and 6-coordination in silicates and oxides [7]. The aim of the present work was to detect possible ionic conductivity in sogdianite ⊥ [001] by AC impedance spectroscopy (IS). As far as we know, this is the first measurement of Li conductivity in milarite-type materials up to date. In order to elucidate corresponding pathways of Li motions, structural changes, particularly in *T*2 and *A* sites, were analyzed by means of Rietveld refinements with neutron powder diffraction data collected in a wide temperature range from 300 to 1273 K.

2. Experimental

2.1. Electron microprobe analysis

A sogdianite sample from Dara-i-Pioz, Tajikistan was obtained at the Munich Mineral Show 2004 from Dr. Victor

Yakovenchuk (Geological Institute, Kola Science Center of Russian Academy of Sciences, Apatity, Russia 184200). The light pink mass of sogdianite consists of mosaic aggregates of parallel arranged platelets. Chemical analysis was performed on a Cameca SX50 electron microprobe apparatus (15 kV, 10 nA). The standards used were albite (Na), corundum (Al), orthoclase (K), hematite (Fe), wollastonite (Si), ilmenite (Ti), and baddeleyite (Zr).

Table 1
Atomic contents of sogdianite obtained by chemical analysis using electron microprobe and occupancies expected for the cation sites of our sample according to [1, 2]

Atom	Atoms per formula unit	Site	Multiplicity in *P6/mcc*	Expected site occupancy
Al	0.03	*A*	4	
Ti^{4+}	0.24	*A*	4	
Fe^{3+}	0.55	*A*	4	
Zr	1.18	*A*	4	0.15[a]
Na	0.36	*B*	8	0.03
K	0.85	*C*	2	0.07
Si	12.00	*T*1	24	1.00
Li	3[b]	*T*2	6	0.25

[a]Sum of occupancies of Al, Ti^{4+}, Fe^{3+}, and Zr at *A* site, when their coherent neutron scattering lengths are normalized with respect to that of Zr.
[b]Calculated by difference on the basis of 30 oxygen atoms per formula unit.

2.2. AC impedance spectroscopy

A plate (width × length × height = $0.09 \times 0.25 \times 0.04\,cm^3$) taken from the sogdianite mass was oriented using an X-ray Laue camera (50 kV, 32 mA). Orientation photographs show the 6-fold rotation axis to be parallel to the "height" and perpendicular to the "length" direction. Therefore, to determine the conductivity perpendicular to the *c*-axis, AC impedance was measured in the "length" direction of the plate. Unfortunately, the small extension of the crystal perpendicular to the "length" direction did not allow further AC impedance measurements parallel to the *c*-axis.

The complex impedance $Z^*(v)$ was recorded with a Hewlett Packard LCR meter (4284 A) in the frequency range 20–10^6 Hz. Both ends of the plate were contacted with Pt paint and then clamped between Pt plates. An NiCr–Ni thermocouple was located close to the sample (~0.3 mm distance), and the sample temperature was maintained to be stable (±1 K) using a temperature controller. The measuring chamber was under N_2 (99.955%) atmosphere throughout the whole experiments. The diluting organic fluid of the Pt paste on the crystal surface was evaporated by heating the cell up to 473 K prior to the start of AC measurements. The AC IS were acquired at intervals of 20 K while heating from 523 up to 1219 K and immediately cooling down to 523 K. The same heating–cooling run was repeated twice in order to ensure the reproducibility of results.

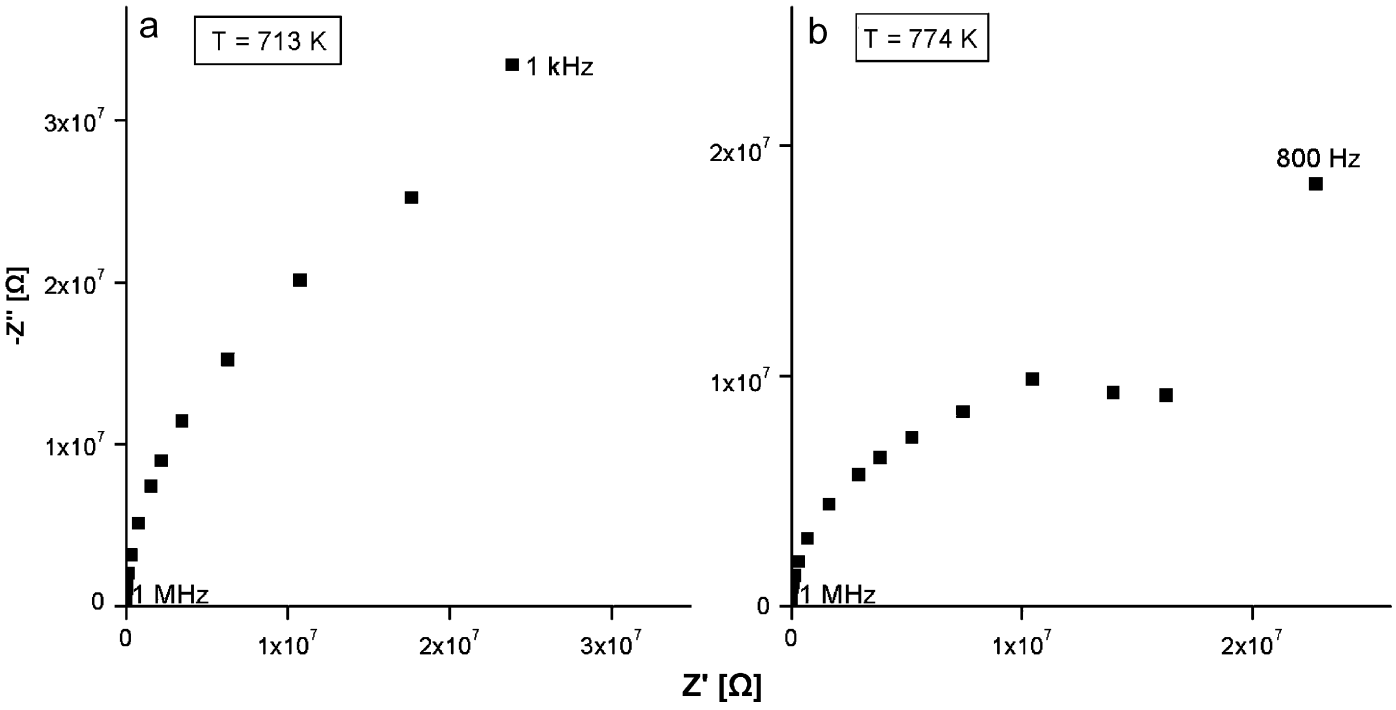

Fig. 2. AC impedance spectra acquired during cooling in the third measurement cycle at 713 K (a), 774 K (b), 894 K (c), 982 K (d), 1129 K (e), and 1213 K (f). Two semicircles (I and II) are clearly resolved in the medium-temperature range (c and d) and superposed at higher temperatures (e and f).

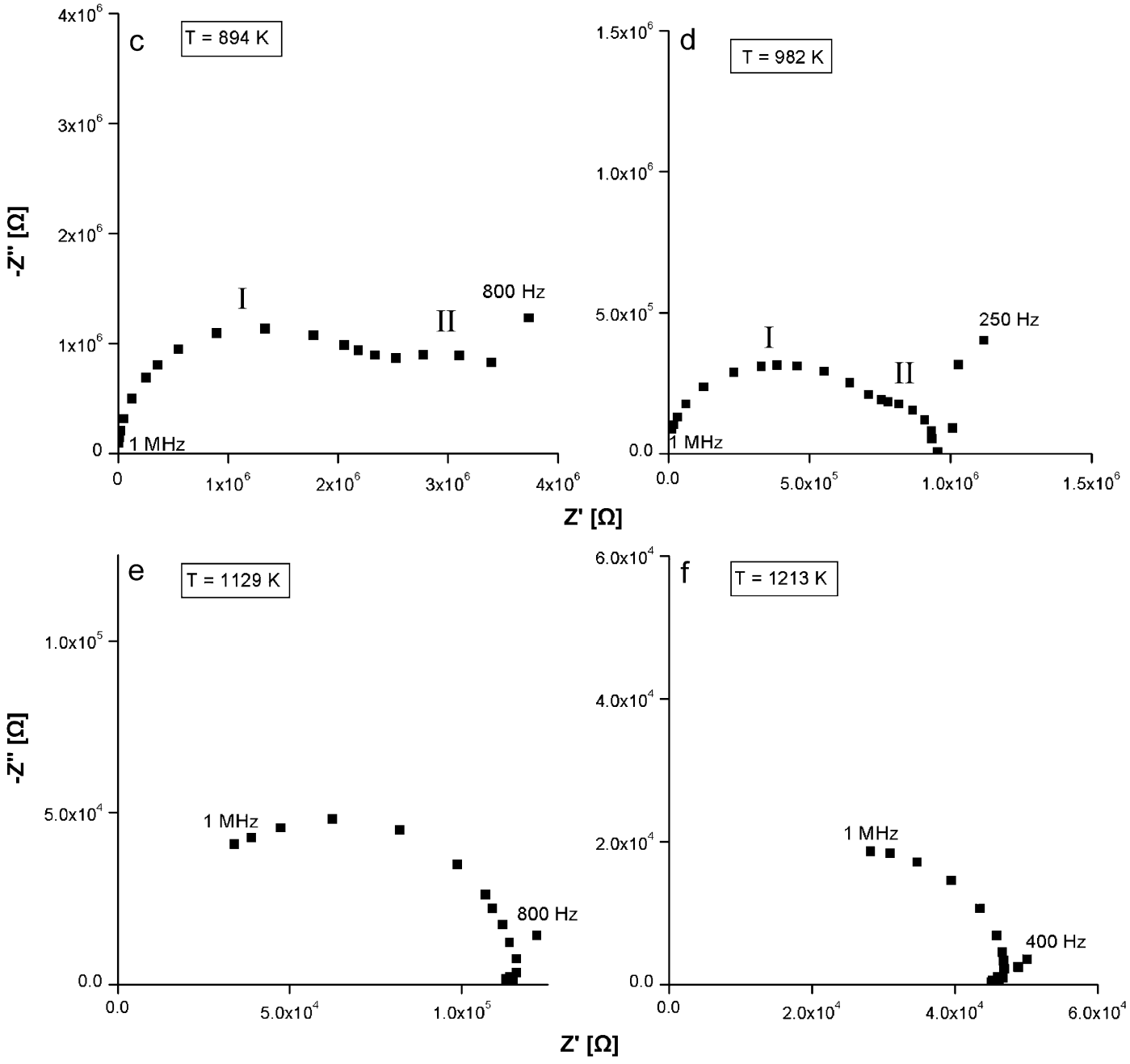

Fig. 2. (*Continued*)

2.3. Neutron powder diffraction

A part of the sogdianite sample (1 g) was finely ground in an agate mortar to collect neutron powder diffraction data. The data collection was carried out with a constant wavelength of 1.549 Å using a Ge(551) monochromator on the instrument SPODI at FRM II, Garching, Germany [8]. The powdered sample was packed in a niobium can, which was accommodated in a high-temperature vacuum Nb furnace. Data were collected by 80 vertically position-sensitive detectors with 300 mm-high collimators. First data sets were obtained at 300, 423, 573, 723, 873, and 1023 K in a 2θ range of 0–160° in steps of 0.05°. These neutron powder patterns were contaminated by a second wavelength of 1.983 Å ($I_2/I_1 = 0.04$), arising from a monochromator problem. After elimination of the second wavelength, a further data set was collected at 1293 K. At each measuring temperature, the data collection was repeated 3–5 times to check the stability of the sample, and these data sets were merged to increase the count rate for better statistics for subsequent structure analysis. Rietveld refinements were carried out using the program package FullProf [9]. Anharmonic atomic displacement parameters (ADPs) were calculated at 1273 K using the program suite JANA2000 [10].

3. Results and discussion

3.1. Chemical analysis

Atomic constituents of our sogdianite sample are listed in Table 1, as resulting from the chemical analysis using electron microprobe. Their distribution on the different crystallographic sites was done by crystal-chemical reasoning in agreement with the previous literatures [1,2]. From this an idealized general formula is derived as $(Zr_{1.18}Fe^{3+}_{0.55}Ti_{0.24}Al_{0.03})(Y_{1.64},Na_{0.36})K_{0.85}[Li_3Si_{12}O_{30}]$, based on 30 oxygen and 3 Li atoms per unit formula. This sogdianite sample contains lower amounts of Al and Na compared with $((Zr_{0.76}\ Fe^{3+}_{0.73}Ti_{0.38}Al_{0.13})(Y_{1.15},Na_{0.85})K[Li_3Si_{12}O_{30}])$ as reported by Cooper et al. [1].

3.2. AC impedance spectroscopy

Plots of the real part Z' against the imaginary part Z'' on the complex impedance plane at various temperatures show semicircles with a low-frequency (LF) tail (Fig. 2a–f). The latter is due to the polarization of the sample/electrode interface [11], indicating ionic conduction in sogdianite. All three of the heating and cooling cycles of AC measurements performed here reveal a single depressed arc below 864 K (Fig. 2a and b). The depressed form of the semicircle indicates variations of relaxation time [12]. Above 864 K, a second semicircle (II) could be distinctively resolved at lower frequencies from the first semicircle (I), as shown in Fig. 2c and d. A semicircle is caused by at least one relaxation mode [12,13], meaning that at least two relaxation processes are involved in ionic conduction perpendicular to the c-axis in the sogdianite sample. The diameters of the semicircles decreasing with increasing temperature point to thermally activated processes. Accordingly, with increasing temperature the resonance frequencies of both semicircles I and II are shifted towards higher frequencies (Fig. 2e and f). This shifting is further presented as a function of the measuring frequency ν by plotting Z'' against $\log \nu$ (Fig. 3). This plot displays two maxima between 864 and 1071 K, being due to two relaxation processes (Fig. 3a). The resonance frequency ν_{res}, i.e., the frequency at the maximum of $Z''(\nu_{res})$, for both I and II is shifted towards higher

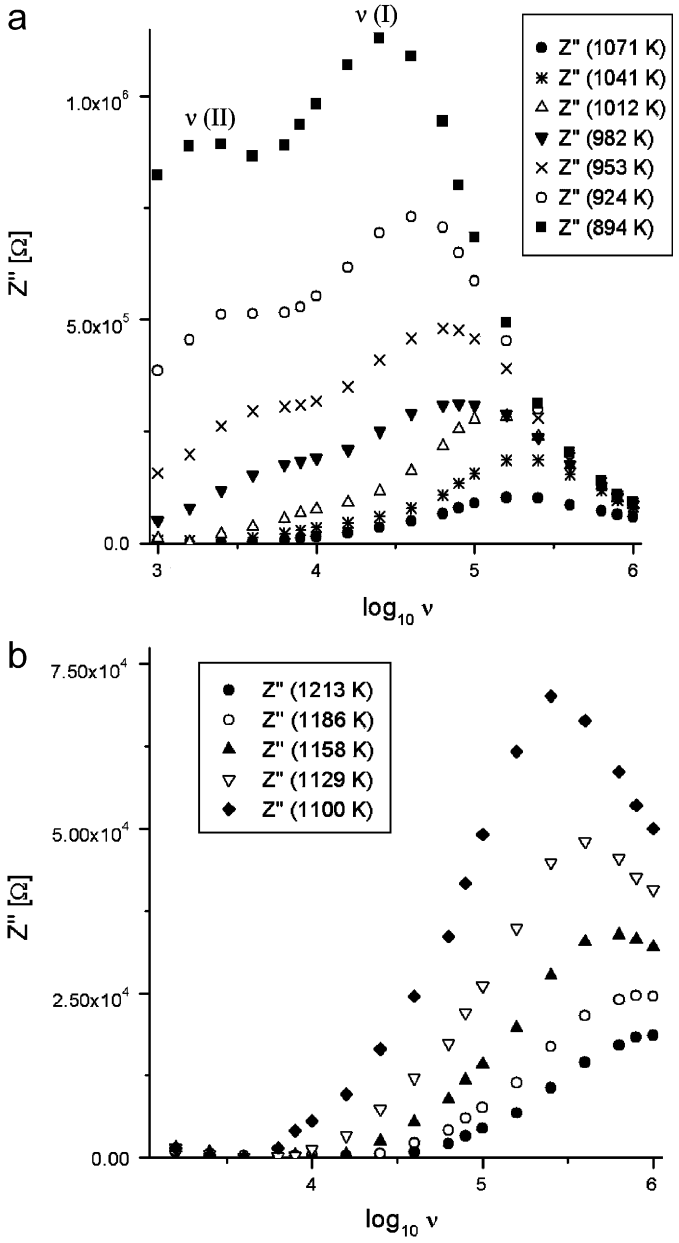

Fig. 3. Plots of imaginary parts Z'' of impedance against $\log \nu$ (ν = AC frequency) in the low-temperature range (a) show that two different resonance frequencies shift towards higher frequencies. At high temperatures above 1100 K (b), the low-frequency resonance moved into the regime of the high-frequency resonance, and finally out of the measuring frequency range above 1213 K.

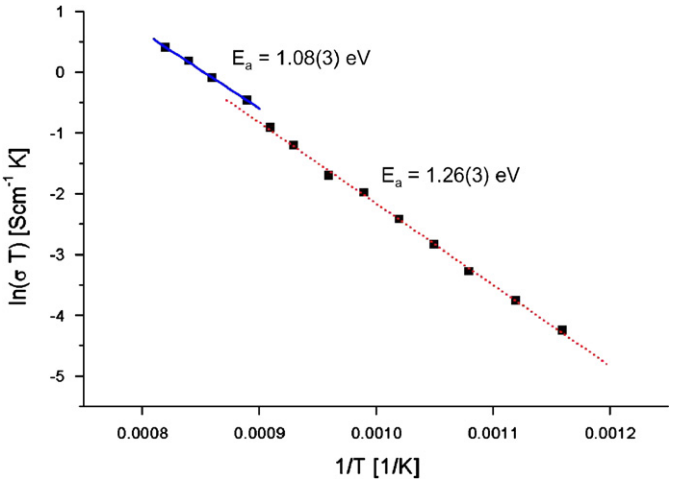

Fig. 4. Arrhenius plot of DC conductivity σ estimated from AC impedance spectra of the third cooling cycle. Two different activation energies (E_a) 1.08(3) and 1.26(3) eV could be determined by linear fit $\ln(\sigma T) = 10.7(3)–12575.7(312.8)(1/T)$ at the high-temperature range and $\ln(\sigma T) = 12.6(3)–14651.8(320.3)(1/T)$ at the low-temperature range, respectively.

Table 2
Results of Rietveld refinements with neutron powder diffractions data of sogdianite in space group $P6/mcc$ and a temperature range of 300–1273 K

	300 K	423 K	573 K	723 K	873 K	1023 K	1273 K
a (Å)	10.0591(2)	10.0576(2)	10.0594(2)	10.0614(2)	10.0653(2)	10.0714(3)	10.0867(4)
c (Å)	14.2508(4)	14.2646(4)	14.2809(4)	14.2947(5)	14.3081(4)	14.3279(6)	14.3873(7)
V (Å^3)	1248.77(4)	1249.63(5)	1251.50(5)	1253.19(6)	1255.35(5)	1258.61(7)	1267.67(9)
R_p (%)	3.26	3.36	3.37	3.68	2.96	3.20	3.56
R_{wp} (%)	4.20	4.28	4.22	4.64	3.71	4.10	4.55
R_{exp} (%)	3.04	3.49	3.20	4.12	2.94	3.04	3.73
χ^2	1.91	1.50	1.75	1.26	1.59	1.82	1.49

$R_p = 100(\Sigma|y_i - y_{c,i}|/\Sigma y_i)$; $R_{wp} = 100(\Sigma w_i|y_i - y_{c,i}|^2/\Sigma w_i y_i^2)^{1/2}$; $R_{exp} = 100[(n-p)/\Sigma w_i y_{c,i}^2]$; $\chi^2 = (R_{wp}/R_{exp})^2$; $w_i = 1/\sigma_i^2$, where σ_i is the standard deviation of the intensity y_i in the observed profile, $y_{c,i}$ the calculated counts, n the total number of data points used in the refinement, and p the number of refined parameters.

Table 3
Final atomic parameters for sogdianite between 300 and 1273 K (B, isotropic atomic displacement parameter in Å^2; β_{ij}, symmetrical matrix representing the anisotropic atomic displacement parameters* in 10^{-4})

	300 K	423 K	573 K	723 K	873 K	1023 K	1273 K
A							
x	1/3	1/3	1/3	1/3	1/3	1/3	1/3
y	2/3	2/3	2/3	2/3	2/3	2/3	2/3
z	1/4	1/4	1/4	1/4	1/4	1/4	1/4
B	1.7(1)						
β_{11}		74(9)	51(8)	58(10)	64(9)	89(13)	108(15)
β_{22}		74(9)	51(8)	58(10)	64(9)	89(13)	108(15)
β_{33}		7(3)	3(3)	16(4)	20(4)	48(6)	46(7)
β_{12}		37(5)	26(4)	29(5)	32(4)	45(7)	54(8)
B							
x	1/3	1/3	1/3	1/3	1/3	1/3	1/3
y	2/3	2/3	2/3	2/3	2/3	2/3	2/3
z	0.481(4)	0.487(7)	0.482(6)	0.478(9)	0.475(7)	0.476(10)	0.476(12)
B	0.5	1.5	2.0	4.0	4.0	5.0	6.0
C							
x	0	0	0	0	0	0	0
y	0	0	0	0	0	0	0
z	1/4	1/4	1/4	1/4	1/4	1/4	1/4
B	0.6(3)						
β_{11}	31(23)	15(24)	39(27)	82(43)	129(39)	129(51)	99(52)
β_{22}	31(23)	15(24)	39(27)	82(43)	129(39)	129(51)	99(52)
β_{33}	1(9)	33(12)	34(12)	99(27)	27(12)	56(21)	125(31)
β_{12}	16(11)	7(12)	20(13)	41(21)	64(19)	65(26)	50(26)
*T*1							
x	0.1158(4)	0.1160(4)	0.1159(4)	0.1156(5)	0.1169(4)	0.1180(6)	0.1174(6)
y	0.3542(4)	0.3550(4)	0.3537(4)	0.3536(5)	0.3550(4)	0.3538(6)	0.3537(6)
z	0.1105(2)	0.1102(3)	0.1098(2)	0.1100(3)	0.1100(2)	0.1093(3)	0.1090(3)
β_{11}	22(5)	34(6)	39(6)	60(8)	43(6)	64(9)	76(10)
β_{22}	48(6)	47(6)	43(6)	37(7)	49(6)	106(10)	91(11)
β_{33}	13(2)	20(2)	25(2)	24(3)	30(2)	31(3)	29(3)
β_{12}	26(4)	24(5)	23(5)	27(6)	23(5)	61(7)	55(8)
β_{13}	−4(3)	−5(3)	−4(3)	−9(4)	−2(3)	3(4)	−9(5)
β_{23}	2(3)	−1(3)	−8(3)	−3(3)	−4(3)	−1(4)	−10(4)
*T*2							
x	1/2	1/2	1/2	1/2	1/2	1/2	1/2
y	1/2	1/2	1/2	1/2	1/2	1/2	1/2
z	1/4	1/4	1/4	1/4	1/4	1/4	1/4
B	1.7(3)						
β_{11}		77(20)	206(41)	270(60)	212(37)	179(41)	238(59)
β_{22}		77(20)	206(41)	270(60)	212(37)	179(41)	238(59)
β_{33}		8(8)	31(12)	39(15)	11(10)	9(11)	63(20)
β_{12}		46(25)	182(46)	246(60)	137(37)	145(48)	187(67)

Table 3 (*continued*)

	300 K	423 K	573 K	723 K	873 K	1023 K	1273 K
O1							
x	0.1305(5)	0.1310(5)	0.1310(5)	0.1316(6)	0.1308(5)	0.1342(7)	0.1309(7)
y	0.3980(5)	0.3979(5)	0.3976(5)	0.4002(6)	0.3978(5)	0.3972(7)	0.3967(7)
z	0	0	0	0	0	0	0
β_{11}	79(8)	93(8)	111(9)	119(10)	132(9)	164(14)	220(15)
β_{22}	94(7)	98(7)	104(7)	156(10)	187(9)	167(12)	185(13)
β_{33}	7(2)	12(2)	19(2)	16(2)	23(2)	26(3)	30(3)
β_{12}	44(7)	48(7)	48(7)	66(9)	72(8)	71(11)	105(12)
O2							
x	0.2218(4)	0.2221(5)	0.2210(5)	0.2214(5)	0.2220(5)	0.2219(7)	0.2214(7)
y	0.2792(4)	0.2796(4)	0.2784(4)	0.2787(5)	0.2786(4)	0.2776(5)	0.2776(5)
z	0.1353(2)	0.1347(2)	0.1347(2)	0.1337(2)	0.1338(2)	0.1329(3)	0.1307(3)
β_{11}	29(4)	52(4)	64(5)	59(5)	78(5)	102(7)	137(8)
β_{22}	49(4)	61(4)	71(5)	97(6)	116(6)	134(8)	155(10)
β_{33}	27(2)	31(2)	30(2)	38(2)	48(2)	62(3)	60(3)
β_{12}	23(4)	35(4)	41(4)	51(5)	64(4)	75(6)	112(8)
β_{13}	−2(2)	−4(3)	−1(3)	−9(3)	1(3)	11(4)	−3(5)
β_{23}	−6(2)	−3(2)	−1(2)	3(3)	1(3)	6(4)	6(4)
O3							
x	0.1608(3)	0.1612(3)	0.1614(3)	0.1617(4)	0.1622(3)	0.1607(4)	0.1632(4)
y	0.5022(3)	0.5019(3)	0.5009(3)	0.5010(4)	0.5006(3)	0.5007(4)	0.5003(4)
z	0.1710(2)	0.1709(2)	0.1707(2)	0.1703(2)	0.1705(2)	0.1705(2)	0.1703(2)
β_{11}	42(4)	61(5)	59(5)	79(6)	87(5)	141(8)	112(9)
β_{22}	41(4)	44(4)	53(5)	53(5)	71(5)	94(7)	96(7)
β_{33}	21(1)	22(1)	23(1)	29(2)	36(2)	40(2)	46(2)
β_{12}	14(4)	24(4	18(4)	23(5)	31(4)	53(7)	54(7)
β_{13}	−1(2)	−6(2)	−2(2)	−4(2)	−11(2)	−17(3)	−19(3)
β_{23}	−5(2)	−7(2)	−11(2)	−12(3)	−25(2)	−18(3)	−25(4)

*Defined as $\beta_{11}h^2+\beta_{22}k^2+\beta_{33}l^2+2\beta_{12}hk+2\beta_{13}hl+2\beta_{23}kl$ with $\beta_{11}=2\pi^2U_{11}a^{*2}$; $\beta_{22}=2\pi^2U_{22}b^{*2}$; $\beta_{33}=2\pi^2U_{33}c^{*2}$ $\beta_{12}=2\pi^2U_{12}a^*b^*\cos\gamma^*$; $\beta_{13}=2\pi^2U_{13}a^*c^*\cos\beta^*$; $\beta_{23}=\pi^2U_{23}b^*c^*\cos\alpha^*$. U is the mean square displacement of atom with respect to the equilibrium position, defining the atomic temperature factor $B=8\pi^2U$.

frequencies with increasing temperature (Fig. 3a). Above 1071 K, the LF resonance coincides with the high-frequency (HF) resonance. Above 1186 K, the resonance frequency exceeds the frequency range of our instrument (Fig. 3b).

For each measuring temperature, the magnitude of the DC conductivity σ was obtained by extrapolating Z'' of the semicircle I for $\omega/2\pi\rightarrow\infty$ onto the Z'-axis towards the LF side on the impedance plane [14]. The DC ionic conductivity values determined at the lower temperature range from 862 to 1069 K are, e.g., 4.1×10^{-5} S cm^{-1} at 923 K and 3.5×10^{-4} S cm^{-1} at 1069 K, reaching a high value of 1.2×10^{-3} S cm^{-1} at 1219 K. By means of an "Arrhenius plot", where the estimated values of σ are plotted logarithmically against $1/T$, activation energies (E_a) for charge transfer processes were estimated. In the temperature range from 862 to 1069 K, an activation energy of 1.26(3) eV ($\approx$122 kJ mol^{-1}) was determined for the HF charge transfer process, which is responsible for the semicircle I (Fig. 4). Another activation energy of 1.08(3) eV ($\approx$105 kJ mol^{-1}) could be determined at the higher temperature range from 1129 to 1219 K (Fig. 4), where only one single resonance frequency was observed.

3.3. Structure refinements with neutron powder diffraction data

Rietveld analysis of the neutron powder diffraction data was started with the model in space group $P6/mcc$ suggested in Ref. [1]. The fair agreement between the calculated and observed powder pattern confirms that the structure is basically the same in our sample. Prior to refining the structure, zero point, cell parameters, and peak-form parameters were refined (Table 2). The Nb reflections from the sample were respected as a second phase.

Rietveld refinements of the crystal structure began with atomic parameters of oxygen and framework $T1$, followed by refining the positional parameter z of the B site. Isotropic ADPs (B) for oxygen, $T1$, A, C, and $T2$ sites were refined simultaneously, while the occupancy parameters of the cation sites were fixed to the contents of the unit cell on the basis of the chemical analysis (Table 1). The occupancy of the A site, at which Zr, Ti^{4+}, Fe^{3+}, and Al are statically disordered, was normalized via their coherent neutron scattering lengths to that of Zr (denoted as "Zr" in the following). The occupancies had to be fixed throughout all refinements due to strong correlations with the ADP (see below).

It was difficult to refine the isotropic ADP (B) for the B site because of its low occupancy. In the entire refinement processes, therefore, these were constrained with the B values obtained for the C site (Table 3), justified by their similar cage-like surroundings in the structure. In the subsequent calculations, anisotropic ADPs (β_{ij}) for oxygen atoms, $T1$, A, C, and $T2$ were included step-by-step. Rietveld refinements at 300 K resulted in a negative value of β_{33} for $T2$ and A. For this reason, only the isotropic ADP is given for $T2$ and A at 300 K in Table 3. The last cycle of Rietveld refinements at all temperatures resulted in good agreement factors $\chi^2 = 1.26$–1.91 (Table 2) between observed and calculated neutron powder patterns. This good agreement is graphically presented for 1273 K in Fig. 5, as an example. The final atomic parameters for each temperature are listed in Table 3.

The lattice expansion of sogdianite with temperature (Table 1) is strongly non-linear with positive thermal volume expansion coefficients $\beta = 9.50 \times 10^{-6}\,K^{-1}$ from 423 to 723 K and $\beta = 2.90 \times 10^{-5}\,K^{-1}$ from 1023 to 1273 K (Fig. 6a). The lattice parameter a contracted slightly from 300 to 423 K and then raised up to 1273 K (Fig. 6b). However, the magnitude of thermal expansion is only 0.2% parallel to [100] between 423 and 1273 K. In contrast, the lattice expansion parallel to [001] (Fig. 6c) is much larger, resulting in a 1.0% expansion of c from 300 to 1273 K. This anisotropic thermal behavior of the material reflects the topology of the tetrahedral framework of double 6MRs densely connected coplanar to $T2O_4$ tetrahedra and AO_6 octahedra parallel to the (001) plane. On the whole, sogdianite is thermally stable as there was no observation of any phase transition up to 1273 K.

At present, it is hard to assign the HF and LF relaxations unambiguously to any intrinsic cationic motions in sogdianite. We have tried to determine the diffusion pathways via refinements with anharmonic ADPs [15], as well as Fourier and difference Fourier maps. Unfortunately, no continuous densities could be clearly detected probably due to limited data qualities. However, strong anisotropies of ADPs of the cations, in particular, Li at $T2$ as well as "Zr" at A may be highly correlated to the ionic conductivity determined with AC IS perpendicular to the c-axis. The ADPs of Li are much larger within (001) plane than parallel to [001] (Fig. 7) in the entire temperature regime (Table 3). Using U_{ij}'s, these anisotropic displacements can be visualized meaningfully, as defining the orientation of the thermal ellipsoid with respect to the crystallographic axes and the magnitude of the three

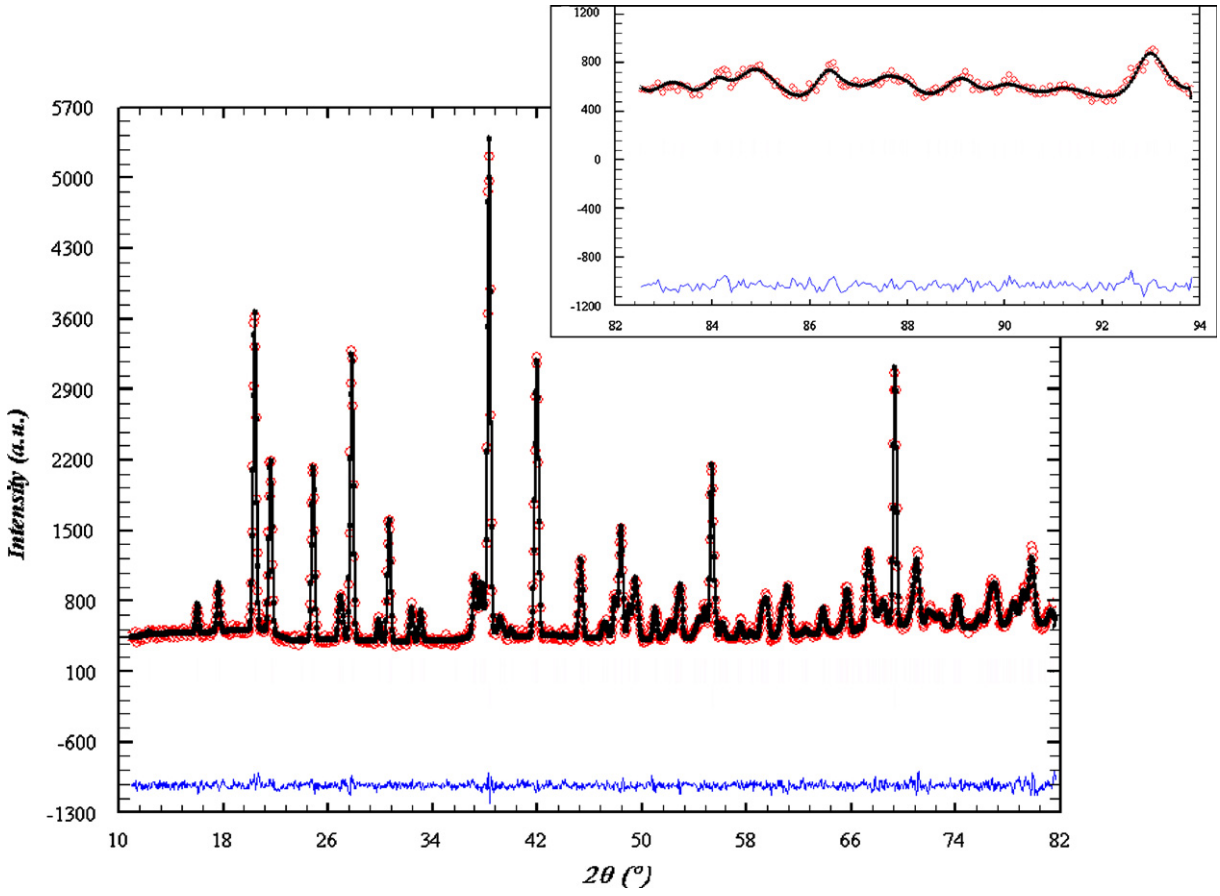

Fig. 5. Calculated (line) and observed (circles) neutron powder diffraction pattern of sogdianite at 1273 K. The upper and lower tickmarks indicate reflections of sogdianite and the Nb can, respectively. The lower curve shows the difference between the observed and calculated data. The plot is enlarged in a limited 2θ range of 82–94° to emphasize good agreement.

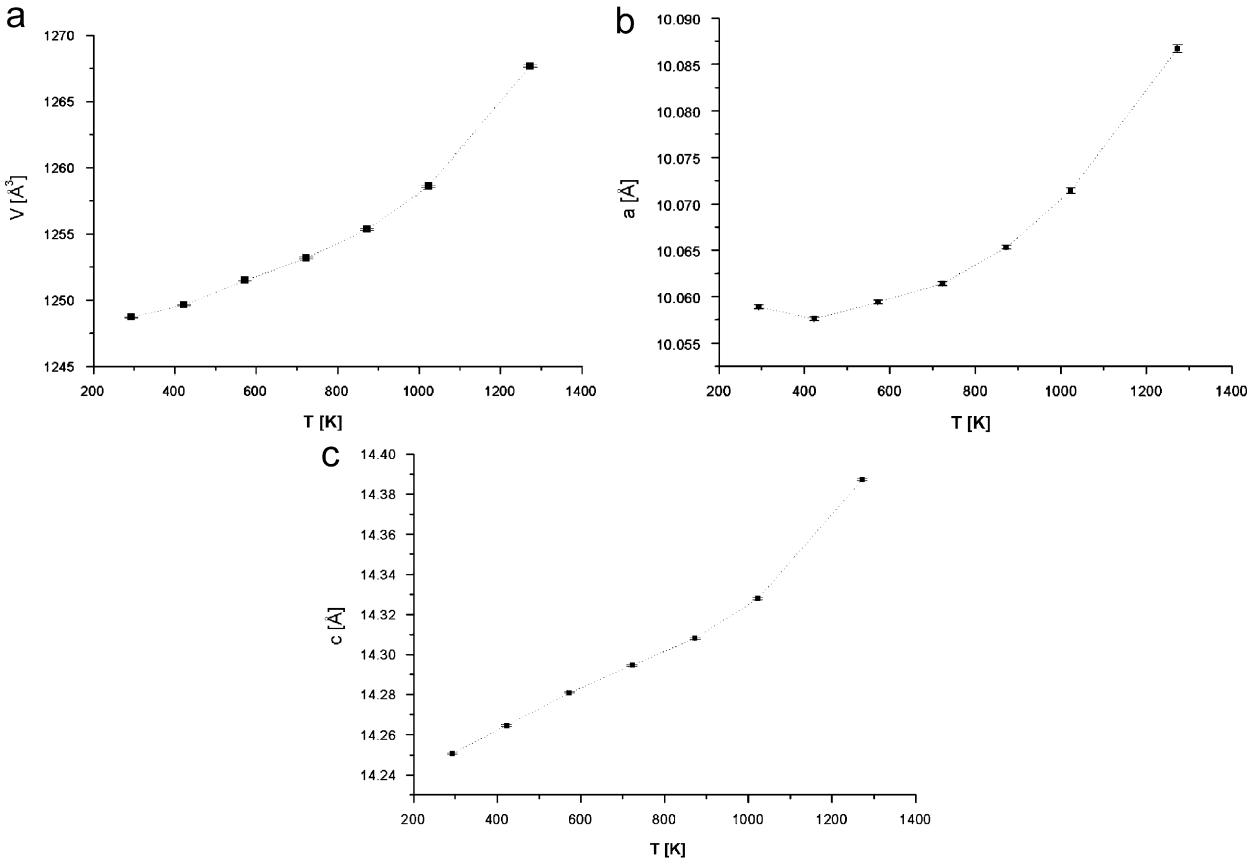

Fig. 6. Thermal expansion of sogdianite between 300 and 1273 K. (a) Volume; (b) *a*; and (c) *c*.

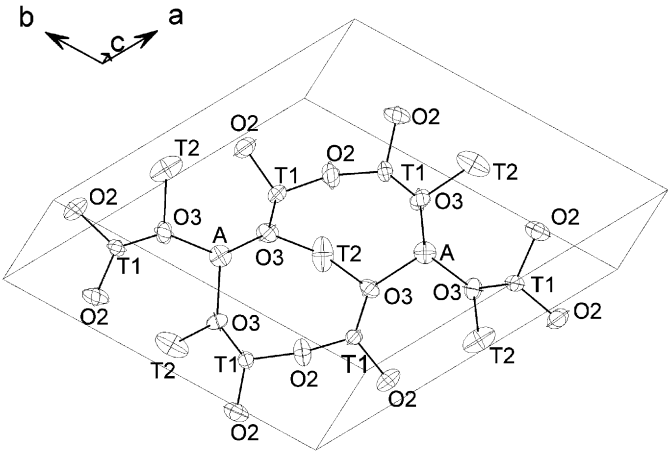

Fig. 7. Structure of sogdianite with ADP ellipsoids at 1273 K.

ellipsoid axes [16]. Figs. 8a and b show the temperature variation of U_{11} and U_{33} of Li and "Zr", respectively. In Fig. 8a, additionally, the mean square displacements along the main axes of the ADP ellipsoids (E_1 and E_2) are indicated (eigenvalues of the U_{ij} matrix). Note that $E_3 = U_{33}$ by symmetry for the *T*2 site, while $E_1 = E_2 = U_{11}$ and $E_3 = U_{33}$ for the *A* site symmetry. Interestingly, between 573 and 723 K both U_{11}(Li) and U_{33}(Li) are deflected markedly from their average increase with temperature towards higher values (Fig. 8a), i.e., where the depressed HF semicircle was clearly detectable in the AC measurements. This behavior may mimic a transient depletion of Li from *T*2 in this temperature range (via strong correlations between occupancies and ADPs).

It is also worth noting that motions of "Zr" at the *A* site are not as large as those of Li at *T*2 (Table 3, Fig. 8b). Moreover, the extrapolation of U_{11}(Zr) towards 0 K gives a large residual ADP value indicating high static displacive disorder, i.e., the various cations appear to be displaced in the *a*,*b* plane. Note that all other extrapolations of U_{11}(Li), U_{33}(Li), and U_{33}(Zr) (here the strong increase at high temperatures had to be modeled with quadratic behavior, see below) roughly go through zero at 0 K, thus confirming our interpretation as a dynamic process. Taking into account, i.e., subtracting the static component of U_{11}(Zr), it is seen that U_{33}(Zr) increases much faster (and even non-linearly) than U_{11}(Zr) (Fig. 8b). This again indicates that, at high temperatures, "Zr" could evade additionally towards the *B* sites which are mostly unoccupied in our sogdianite (Fig. 9). The anomalous increase of the lattice expansion parallel to *c* in the high-temperature region (Fig. 6c) could support the view of the motion of "Zr" from *A* towards *B*. As a consequence, Li can jump over partially empty *A* sites via a vacancy mechanism. The larger values of U_{33}(Li) and U_{33}(Zr) at high temperatures can be taken as being due to a depletion of the occupancies at *T*2 and *A*, respectively. It should be mentioned that we

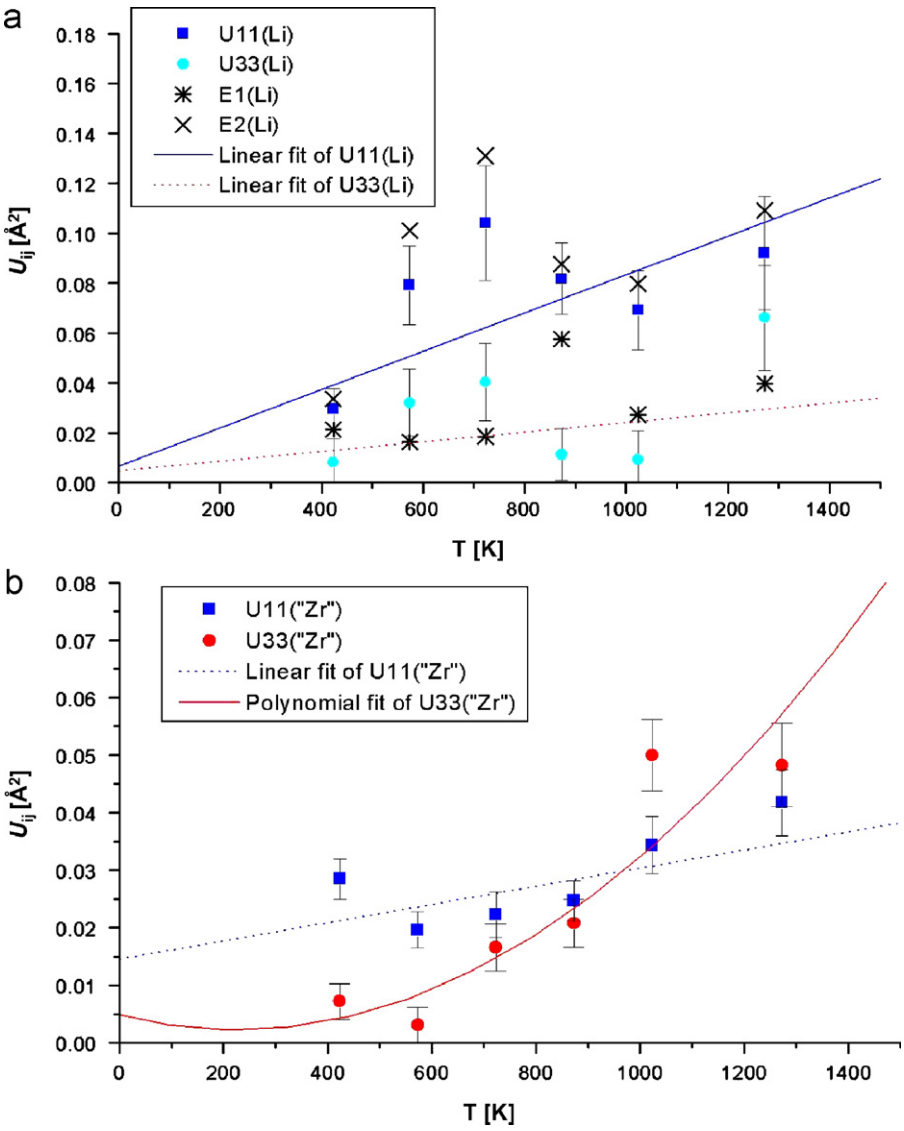

Fig. 8. ADPs U_{11} and U_{33} of Li and "Zr" at $T2$ (a) and A site (b). In (a) the mean square displacements E_1 and E_2 along the main ellipsoid axes (oriented along $a+b$ and $a-b$, respectively) in the $a-b$ plane are added.

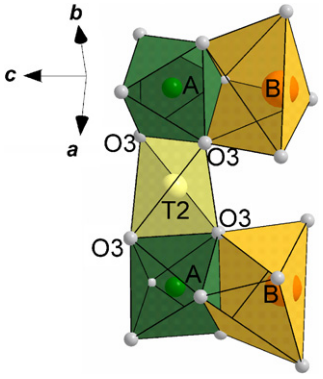

Fig. 9. Local configuration of $T2$, A, and B sites illustrating the possible ways for ionic charge transfer in sogdianite.

have tried to refine the occupancies of these sites (A, B, and $T2$) to support these conclusions. Although there were indeed hints in this direction, the resulting large errors due to the correlation with the ADPs did not allow a definite conclusion.

Therefore, apart from these features, any further details about Li dynamics in sogdianite cannot be proposed. Nonetheless, some general conclusions on the diffusion process can be drawn. The Li-ionic conductivity in sogdianite seems to be intimately correlated with the situation at the A site. Note that above 864 K, where U_{33}(Zr) profoundly exceeds U_{11}(Zr) (Fig. 8b), the LF semicircle could be distinctively resolved in the AC spectra. These observations may point towards a site exchange process of Li from $T2$ via A sites at high temperatures, and support an assignment of this LF relaxation mode to this site exchange process. Jumps of Li directly to B and C sites seem to be less probable due to much longer distances. On the other hand, at low temperatures it is not possible to completely exclude motions of any other cations (in particular Na) beside the depletion of Li from $T2$, as well

Table 4
Selected interatomic distances (Å) and angles in sogdianite between 300 and 1273 K

		300 K	423 K	573 K	723 K	873 K	1023 K	1273 K
A–O3	× 6	2.036(2)	2.036(2)	2.041(2)	2.044(3)	2.043(2)	2.050(3)	2.048(3)
B–O1	× 3	2.455(7)	2.445(8)	2.45(1)	2.44(2)	2.46(1)	2.46(2)	2.48(2)
B–O3	× 3	2.75(4)	2.82(8)	2.76(7)	2.7(1)	2.71(8)	2.7(1)	2.7(1)
C–O2	× 12	3.045(3)	3.053(3)	3.045(3)	3.057(3)	3.059(4)	3.061(4)	3.086(4)
*T*1–O1		1.622(3)	1.617(4)	1.617(4)	1.627(5)	1.621(3)	1.612(5)	1.615(5)
*T*1–O2		1.623(7)	1.627(7)	1.618(7)	1.618(9)	1.623(7)	1.61(1)	1.61(1)
*T*1–O2[a]		1.617(4)	1.619(5)	1.619(5)	1.613(5)	1.620(5)	1.625(7)	1.615(7)
*T*1–O3		1.578(5)	1.570(5)	1.574(5)	1.570(6)	1.560(5)	1.582(7)	1.579(7)
O1–*T*1–O2		110.2(4)	109.7(5)	110.3(5)	110.1(5)	109.9(5)	109.4(7)	109.2(6)
O1–*T*1–O2[a]		110.5(3)	110.4(3)	110.6(3)	110.5(4)	109.7(3)	110.1(4)	108.7(4)
O1–*T*1–O3		109.3(3)	109.9(3)	109.6(3)	108.6(3)	110.0(3)	110.0(4)	110.2(4)
O2–*T*1–O2[a]		104.9(4)	104.8(5)	104.6(5)	105.1(5)	104.7(5)	104.8(7)	105.3(7)
O2–*T*1–O3		112.0(5)	111.8(5)	111.7(5)	112.0(6)	112.1(5)	113.1(7)	112.5(7)
O2[a]–*T*1–O3		109.9(3)	110.1(3)	109.9(3)	110.6(4)	110.4(3)	109.4(5)	110.8(4)
*T*2–O3	× 4	1.962(3)	1.969(3)	1.976(3)	1.982(4)	1.988(3)	1.979(4)	2.005(4)
O3–*T*2–O3[a]	× 2	110.0(3)	110.0(3)	110.1(3)	109.8(3)	110.2(3)	109.6(3)	110.2(3)
O3–*T*2–O3[a]	× 2	132.7(3)	132.6(3)	132.1(3)	132.2(4)	131.9(3)	132.2(4)	131.7(4)
O3–*T*2–O3[a]	× 2	88.9(2)	88.9(2)	89.2(2)	89.4(2)	89.3(2)	89.6(2)	89.4(2)
A–*T*2		2.904	2.903	2.904	2.905	2.906	2.907	2.912
A–*B*		3.3(1)	3.4(1)	3.3(1)	3.3(1)	3.3(1)	3.3(1)	3.3(2)
B–*B*		0.5(1)	0.4(1)	0.5(1)	0.6(1)	0.7(1)	0.6(2)	0.7(2)
*T*1–*T*2		3.028(3)	3.027(4)	3.041(5)	3.039(5)	3.040(4)	3.065(6)	3.073(6)
A–O3–*T*2		93.1(1)	92.9(1)	92.6(1)	92.3(1)	92.2(1)	92.4(1)	91.8(1)
O3–*A*–O3[a]		84.9(2)	85.3(2)	85.7(2)	86.0(2)	86.3(2)	85.7(2)	87.0(2)
O3–*T*2–O3[a]		88.9(2)	88.9(2)	89.2(2)	89.4(2)	89.3(2)	89.6(2)	89.4(2)

[a]Symmetrically equivalent site.

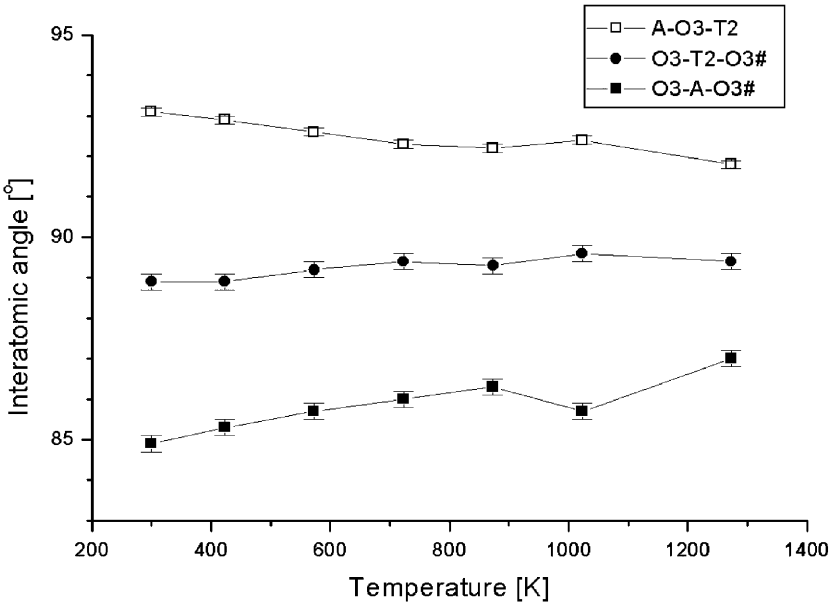

Fig. 10. Temperature dependence of interatomic angles ∠(*A*–O3–*T*2), ∠(O3–*T*2–O3$^{\#}$), and ∠(O3–*A*–O3$^{\#}$) in sogdianite ($^{\#}$: symmetrically equivalent).

as charge transfer between mosaic boundaries of the crystal in the assignment of the HF relaxation mode. Furthermore, because of the static disorder at the *A* site and the large errors of anisotropic temperature parameters of Li, the way of charge transfer in sogdianite suggested here must be regarded as tentative only.

The suggested mechanism of Li hopping from *T*2 over *A* sites is further supported geometrically by the short distance of ≈2.9 Å between edge-sharing $T2O_4$ tetrahedra and AO_6 octahedra (Fig. 9). From 300 up to 1273 K, the distance between *T*2 and *A*, *d*(*T*2–*A*), increased only from 2.904 to 2.912 Å (Table 4), which corresponds to the low

degree of the lattice expansion parallel to *a*. Comparably, these distances are much smaller [7] than those between two neighboring LiO_4 tetrahdra being about 3.4 Å in a corner-sharing configuration, often occurring in Li-ionic silicate and oxide conductors [17–19]. Attention should be paid to the directions of the Li and "Zr" movements. Their probability densities do not indicate the direct path straight across their shared edges, but an indirect and more spacious pathway through the faces of the edge-sharing $T2O_4$ tetrahedra and AO_6 octahedra (Figs. 7 and 9). The former case seems to be unrealizable in sogdianite because of the narrow bottle neck ($\approx$2.82 Å) between two oxygen atoms at the edge shared by $T2O_4$ and AO_6 (Fig. 9). With increasing temperature, the bridging angle $\angle(A\text{–}O3\text{–}T2)$ markedly decreases with concomitant enlargements of both bonding angles $\angle(O3\text{–}A\text{–}O3)$ and $\angle(O3\text{–}T2\text{–}O3)$ (Table 4; Fig. 10). The steady decrease of the bridging angle $\angle(A\text{–}O3\text{–}T2)$ maintains not only the low increase in the ($T2$–A) distance, but also ensures short pathways for the site exchange of Li between $T2O_4$ and AO_6 polyhedra. These geometrical changes compensate the positive thermal expansion of the lattice to keep Li hopping easy via short pathways. In addition, the presence of vacancies at the *B* site is also advantageous for the cationic conductivity in sogdianite: A part of AO_6 octahedra can be emptied, at least transiently, when *A* cations hop parallel to *c* towards neighboring unoccupied *B* sites providing a reasonable 6-fold coordination with oxygen atoms also for *A* cations (Fig. 9). As mentioned above, the strong increase of U_{33}(Zr) above 864 K (Fig. 8b) supports this possibility. These vacancies are a necessary prerequisite to allow a fast Li diffusion on the *a*,*b* plane.

In conclusion, the results of our Rietveld analysis with neutron powder diffraction data collected at $T = 300$–1273 K can explain the LF semicircle in AC IS spectra measured perpendicular to the *c*-axis as a consequence of the site exchange of Li between $T2$ and *A* sites. This charge transfer process via vacancies requires to overcome an energy barrier of 108(3) eV and becomes dominant at high temperatures. Sogdianite has a DC conductivity value of 1.2×10^{-3} S cm^{-1} at 1219 K, and therefore could be applied as a high-temperature superionic conductor. Further elucidation of the mechanism of charge transfer over the lattice of sogdianite requires synthesis works on sogdianite variants with simplified chemical contents. IS measurements in various directions with larger single crystals with high quality are desired in order to assign the HF relaxation mode observed in this study. These on-going works are in progress at the aim of developing Li-bearing milarite-type materials with higher ionic conductivity.

Acknowledgment

We acknowledge financial support from the DFG via PA 1222/1-1 (SHP). We thank Mr. Peter Dreier and Mr. Hilger Lohringer for support of the chemical analysis using electron microprobe.

References

[1] M.A. Cooper, F.C. Hawthorne, E.S. Grew, Am. Miner. 84 (1999) 764–768.
[2] E.V. Sokolova, F.C. Hawthorne, Can. Miner. 38 (2000) 853–859.
[3] F.C. Hawthorne, M. Kimata, P. Černý, N. Ball, Am. Miner. 76 (1991) 1836–1856.
[4] Th. Armbruster, R. Oberhänsli, Am. Miner. 73 (1988) 596–600.
[5] T. Kato, Y. Miuara, N. Murakami, Miner. J. 8 (1976) 184–192.
[6] L.A. Pautov, A.A. Agakhanov, Zap. Vser. Miner. Obshchest. 126 (4) (1997) 75–80.
[7] R.D. Shannon, Acta Crystallogr. A 32 (1976) 751–767.
[8] R. Gilles, M. Hoelzel, M. Schlapp, F. Elf, B. Krimmer, H. Boysen, H. Fuess, Z. Kristallogr. Suppl. 23 (2006) 183–188.
[9] FullProf 2000, Version July 2001, J. Rodrígues-Carvajal, Laboratoire Léon Brillouin (CEA-CNRS), France.
[10] JANA 2000, Version December 2005, V. Petricek, M. Dusek, Institute of Physics, Academy of Sciences of the Czech Republic, Praha.
[11] U. Simon, M.E. Franke, Micropor. Mesopor. Mater. 41 (2000) 1–36.
[12] J.R. Macdonald, Impedance Spectroscopy, Wiley, New York, 1987.
[13] K.L. Ngai, C. León, Phys. Rev. B 60 (13) (1999) 9396–9405.
[14] Y.T. Tsai, D.H. Whitmore, Solid State Ionics 7 (1982) 129–139.
[15] H. Boysen, Z. Kristallogr. 218 (2003) 123–131.
[16] C. Giacovazzo, H.L. Monaco, D. Viterbo, F. Scordari, G. Gilli, G. Zanotti, M. Catti (Eds.), Fundamentals of Crystallography, International Union of Crystallography, Oxford Science Publication, 1991.
[17] A.D. Robertson, A.R. West, A.G. Ritchie, Solid State Ionics 104 (1997) 1–11.
[18] L. Sebastian, A.K. Shukla, J. Gopalakrishnan, Proc. Indian Acad. Sci. (Chem. Sci.) 113 (5&6) (2001) 427–433.
[19] M. Nakayama, Y. Ishida, H. Ikuta, M. Wakihara, Solid State Ionics 117 (1999) 265–271.